Electrochemistry Hot Paper

Direct Detection of Surface Species Formed on Iridium Electrocatalysts during the Oxygen Evolution Reaction

Arjun BalaKrishnan, Niclas Blanc, Ulrich Hagemann, Parham Gemagami, Kevin Wonner, Kristina Tschulik,* and Tong Li*

Abstract: *The effect of surface orientations on the formation of iridium oxide species during the oxygen evolution reaction (OER) remains yet unknown. Herein, we use a needle-shaped iridium atom probe specimen as a nanosized working electrode to ascertain the role of the surface orientations in the formation of oxide species during OER. At the beginning of electrolysis, the top 2–3 nm of (024), (026), (113), and (115) planes are covered by IrO–OH, which activates all surfaces towards OER. A thick subsurface oxide layer consisting of sub-stoichiometric Ir–O species is formed on the open (024) planes as OER proceeds. Such metastable Ir–O species are thought to provide an additional contribution to the OER activity. Overall, this study sheds light on the importance of the morphological effects of iridium electrocatalysts for OER. It also provides an innovative approach that can directly reveal surface species on electrocatalysts at atomic scale.*

Introduction

The development of affordable, sustainable, and environmentally friendly energy conversion and storage technologies is critical for meeting ever-increasing energy demands. Water electrolysis, when combined with renewable electricity generation technologies such as photovoltaic cells, is expected to emerge as a low-emission method of sustainable energy storage and hydrogen production.[1] However, the targeted

efficiency of water electrolysis presents an ongoing challenge, mainly due to limitations in electrocatalyst performance at the anode, where the oxygen evolution reaction (OER) takes place.[2] Metallic iridium (0, Ir) and iridium($+IV$) oxide (IrO_2) exhibit the best combination of activity and long-term stability towards OER in acidic media.[3] A better understanding of the origin of the outstanding performance of Ir and IrO_2 is key to improve the design of high-performance OER catalysts for large scale industrial application, which potentially necessitate the replacement of Ir with more earth-abundant and affordable elements.

To date, the dependence of OER activity and stability on surface orientations of Ir-based catalysts remains poorly understood.[4] Özer et al. showed that the Ir (110) single crystal is more active than the (111) single crystal, suggesting that the activity difference is possibly due to the fact that the open and accessible (110) planes enable faster oxidation in the initial OER stages compared to the closed (111) planes.[5] In contrast, Scohy et al. claimed that the initial arrangement of crystallographic orientations is not necessarily important to either activity or stability because the individual surfaces of Ir electrocatalysts all evolve into similar final inactive surface states in terms of OER activity.[6] Despite efforts in this research area, there is currently a lack of consensus regarding the role of the Ir surface orientation in OER activity and stability. This knowledge gap has hindered the optimization of Ir electrocatalysts through the control of nanoparticle shape, to improve their surface-specific catalytic activity.[7] Therefore, optimizing the Ir electrocatalysts via the shape control approach requires a better understanding of the interplay between structure, activity, and stability of various Ir surface facets under the OER conditions.

The conflicting literature evidence of morphological effects of Ir possibly originates from the fact that OER activity cannot be unambiguously correlated to initial surface structure since catalyst surface states undergo dramatic changes during OER. Additionally, it is challenging to simultaneously perform direct and surface-sensitive measurements during electrochemical reactions. A range of powerful surface techniques, including in situ near-ambient pressure X-ray photoelectron spectroscopy (XPS),[9] X-ray photoemission and absorption spectroscopies,[8] and X-ray absorption near-edge structure,[9] have provided valuable information regarding the surface species formed during OER. However, most methods measure the average electronic state of the top ca. 5 nm of a surface with limited or low spatial resolution. The inability to perform a full three-dimensional (3D) structural and chemical characterization of surfaces and

[*] A. BalaKrishnan, P. Gemagami, Prof. Dr. T. Li
Institute for Materials, Ruhr-Universität Bochum
Universitätsstrasse 150, 44801 Bochum (Germany)
E-mail: tong.li@rub.de

N. Blanc, K. Wonner, Prof. Dr. K. Tschulik
Faculty of Chemistry and Biochemistry
Analytical Chemistry II, Ruhr-Universität Bochum
Universitätsstrasse 150, 44801 Bochum (Germany)
E-mail: kristina.tschulik@rub.de

Dr. U. Hagemann
Interdisciplinary Center for Analytics on the Nanoscale (ICAN) and
Center for Nanointegration Duisburg-Essen (CENIDE)
University of Duisburg-Essen
Carl-Benz-Strasse 199, 47057 Duisburg (Germany)

near-surface regions of an electrocatalyst impedes the complete evaluation of the contribution made by individual atoms in this extended zone to the interplay of catalytic activity, selectivity, and stability. There is, therefore, an urgent need to complement these state-of-the-art surface techniques for a 3D analytical approach that is genuinely capable of surface-sensitive measurement of composition and elemental distribution.

Atom probe tomography (APT) can provide uniquely powerful insights into the atomic-scale composition and structure of materials in 3D, which has been employed to characterize catalyst nanoparticles and nanocrystals,[10] and for model catalyst studies.[11] The APT specimen takes the form of a needle-shaped sample whose tip has a diameter in the range 30–100 nm and can therefore directly be used as a working electrode in electrochemical studies. Additionally, a considerable number of planes and facets that are exposed on the APT tip makes it an ideal model system in which to study the influence of different facets on the formation of surface species during OER.[12] In other words, one does not need to perform experiments on single crystals in order to investigate the role of surface facets in the reactivity.[5,6] Previously, APT specimens have been used to investigate surface changes on the Pt–Rh (002), (220), (024), and (111) planes following exposure to oxidizing gases (NO and O_2)[11e,13] and thermal oxidation at high temperatures.[14] These previous investigations focused on the surface changes that take place during gas–solid reactions. In the present study, we will utilize the APT specimen to pioneer the investigation of surface species formed during liquid–solid reactions. Specifically, we will combine APT with XPS to probe the surface species that are present on the Ir electrodes in order to obtain novel insights into surface changes that take place on the Ir (002), (026), (024), (113), (115), (220), and (111) planes during OER. Such atomic-scale information will, in turn, assist in the design of high-performance Ir catalyst nanoparticles of optimum shape for OER to make most-efficient use of this scarce element.

Results and Discussion

Here, we develop an approach to examine the electrochemical properties, electronic state, and surface chemistry of the surfaces of the same nanosized electrode, i.e., the atom probe specimen. APT specimens were prepared by electropolishing of "as drawn" Ir wire in a chemical solution of one part of saturated $CaCl_2$ and two parts of deionized water. The surfaces of the APT specimens were subsequently cleaned of residual oxides by field evaporation in APT and HCl before being exposed to electrochemical characterization. The thus obtained iridium nanotips served as working electrodes for subsequent electrochemical studies. Although all APT specimens were prepared according to the same protocol, it is impossible to avoid inter-sample variations in tip radius and shank angle. As a result, the electrochemically active surface area of the tips may vary when they are immersed in an electrolyte. Interpretation and comparison of the electro-

chemical data under varying experimental conditions is thus challenging.

We addressed this challenge by measuring the tip surface area that was in contact with the electrolyte in order to normalize the electrochemical currents obtained in different experiments. At least three independent experiments were performed for each data point. Specifically, we first inspected the size and morphology of the topmost 500 μm region of the APT tip using scanning electron microscopy (SEM, Figure 1 a). The electrochemically active surface area of each specimen, that is, each working electrode in the subsequent OER experiments, was initially determined. To this end, we combined electrochemical calibration experiments in 5 mM $K_4[Fe(CN)]_6$ and 100 mM KCl electrolyte solutions at a potential of 0.4 V versus a silver/silver chloride reference electrode (Ag/AgCl, 3 M KCl, $E = 0.21$ V vs. standard hydrogen electrode) at an immersion depth of 500 μm (controlled by a micrometer-screw) with numerical finite element simulations (Figure 1 b–d). The simulations were used to obtain the immersed surface area of each tip based on its SEM-derived shape (see Figure S1) by fitting numerically simulated chronoamperogram data to the recorded calibration current curves, as shown in Figures 1 c,d. Despite the inherent shape difference of the prepared Ir nanotips, the difference in electrochemically probed surface area was found to be less than eight percent for the specimen analyzed in this work (see Figure S2).

Next, the APT specimens were electrochemically oxidized in 0.1 M $DClO_4$ in D_2O for 60, 180, and 300 seconds at 1.55 V versus a reversible hydrogen electrode (RHE) at pH 1.0, where OER takes place (Figure 1 e).[15] Potentials were measured versus a Ag/AgCl reference electrode and are reported against RHE for ease of comparison to other work ($E_{RHE} = E_{Ag/AgCl} + 0.197 + 0.059$ pH). Measured oxygen evolution current response was normalized by the surface area of each tip, determined as described above. The derived current densities were similar for all specimens (see Figure 2), and show a typical chronoamperometric curve: a steep initial decrease is followed by a more gradual decrease (at ca. 60 s), finally reaching a plateau of approximately 2.5 A m^{-2} at about 280 s.

Following these electrochemical measurements, the surface state of the APT specimen was measured by XPS (Figure 1 f). Although XPS usually requires a flat specimen, we proved the feasibility of using, instead, a needle-shaped specimen.[16] The results of this feasibility test are shown in Figure S3, where a circular region with a diameter of 20 μm from an APT tip was analyzed (Figure S3a,b) after OER for 60 and 300 seconds, respectively. Despite the comparably low signal-to-noise levels of this experiment, the XPS data in Figure S3c,d clearly show Ir 4f spectra, at 60.9 and 63.9 eV,[17] demonstrating the feasibility of analyzing needle-shaped APT specimens by XPS. The peaks at 61.9 and 64.9 eV (Figure S3c) can be assigned to Ir(+IV) species,[15a,18] and those at 62.5 and 65.5 eV to Ir(+III) and/or Ir(+V) species[9,19] (the strong overlap of signals of those two species prohibits further distinguishing them). For samples catalyzing OER for 60 s (Figure S3c), more Ir(+III) species (approx. 2% of the total Ir signal) are present on the APT specimen surface and about
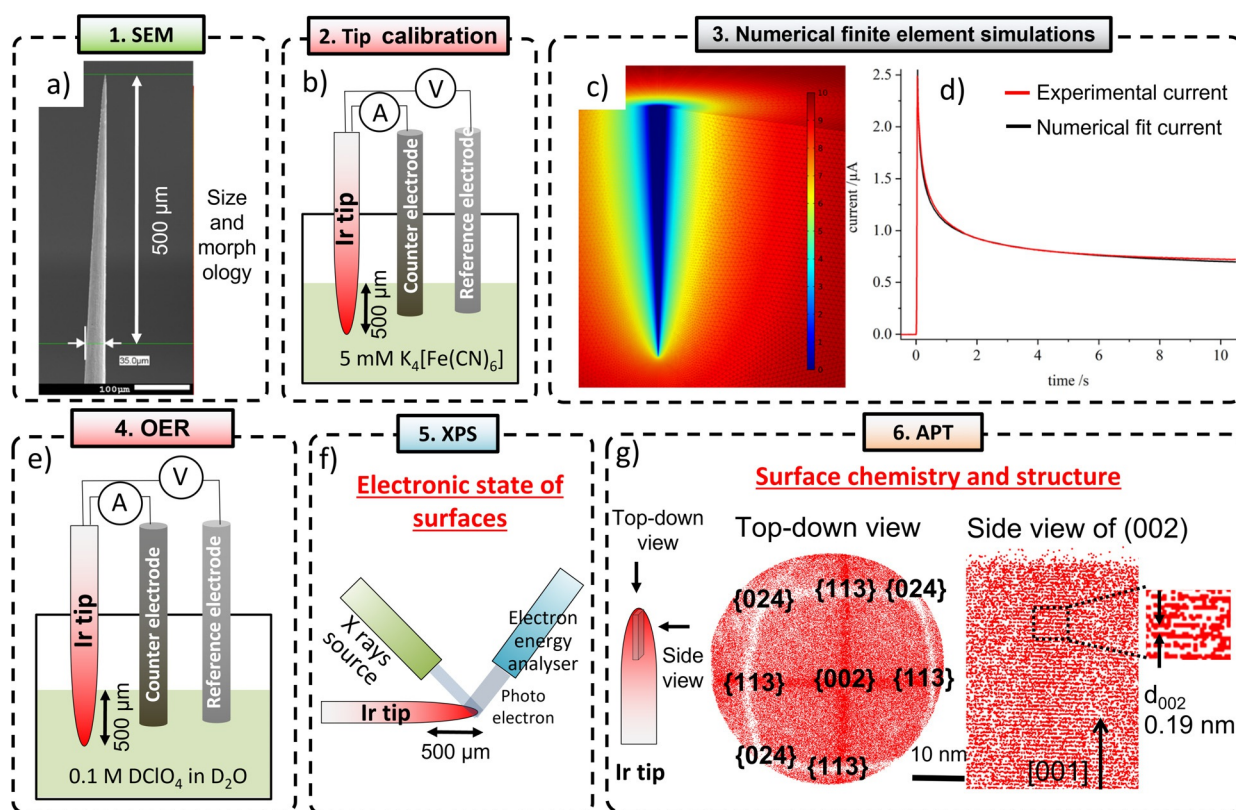
Figure 1. The workflow includes a) step 1: SEM measurement of size and morphology of the Ir APT tip, b) step 2: chronoamperometric measurements of the Ir APT tip in solutions of 5 mM $K_4[Fe(CN)_6]$ at an immersion depth of 500 μm, followed by step 3: c) revolved numerical finite element simulation of the concentration and d) simulated and experimental currents, e) step 4: electrochemical OER measurement performed on the APT tip at the same immersion depth as in step 2, f) step 5: XPS measurement of the top ca. 20 μm region of the APT specimen, and g) step 6: APT experiment of the same tip in the previous steps (the top-down view of the APT reconstruction of an unoxidized Ir APT tip showing a number of different crystal planes on the apex and the side view revealing the interplanar spacing of (002) planes).
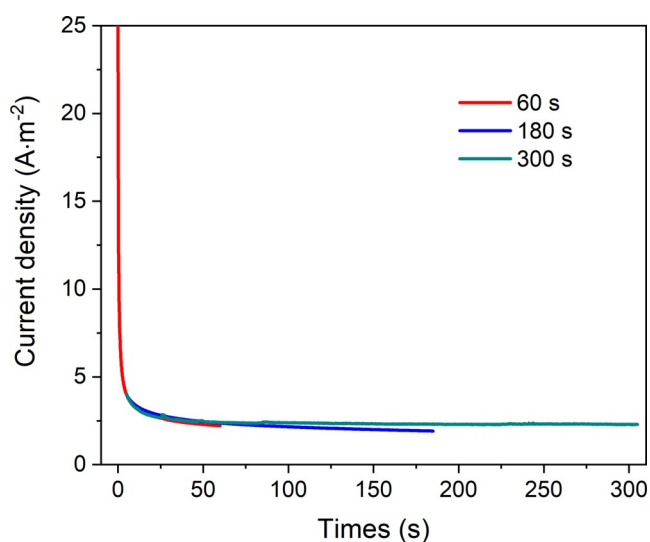

Figure 2. Chronoamperogram of the APT specimens treated for 60, 180, and 300 s in 0.1 M $DClO_4$ at 1.55 V vs. RHE at pH 1. The surface areas of the APT specimens were determined via numerical simulation shown in Figure 1 c,d (details described in the SI).

4% Ir(+ IV) species are detected, while most of the surface remains metallic in nature (95% of the total Ir signal). After

300 s of OER experiments (Figure S3d), the Ir(+ III) and/or Ir(+ V) species decreased to less than 0.5%. This is only an upper limit of the Ir(+ III/ + V) content as the signal cannot be clearly seen within the noise of the data after 300 s of OER. Additionally, the ratio of Ir(+ IV) species to metallic Ir^0 increased to approximately 10% of the total Ir signal, indicating that additional Ir(+ IV) species form during 300 s of anodic tip oxidation. This result is in agreement with previous reports on anodically polarized Ir films.[20] It should be pointed out that at 300 s, still a high fraction of metallic Ir^0 (approx. 90%) was detected by XPS analysis.

After examining the surface oxidation states by XPS, we next used APT to determine the effect of crystallographic planes on the formation of oxide species during OER. APT data take the form of a 3D point cloud, whereby every point represents an atom/ion that has been individually detected and identified.[21] The needle-shaped APT tip offers multiple crystallographic planes for investigation, as indicated by the top-down view in Figure 1 g. The poles and zone lines can be identified from either low or high atomic densities since the trajectories of ions evaporated from crystallographic planes are affected by localized electric field variations.[22] Guided by stereographic projection diagrams, Miller indices can be assigned to the crystallographic poles, as seen in the top-down views of APT reconstructions of an unoxidized Ir tip and
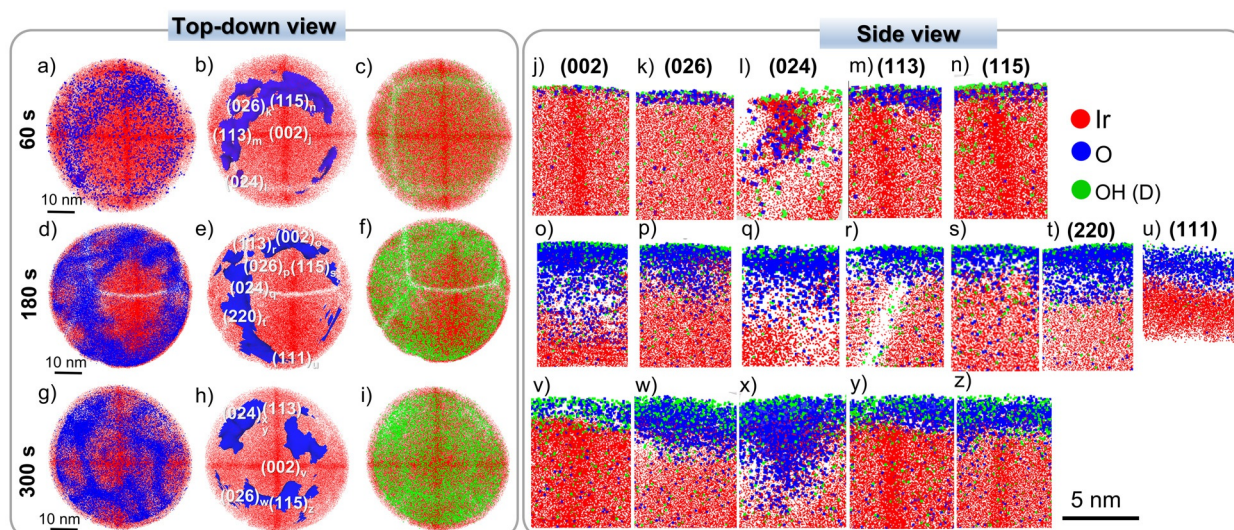
Figure 3. Top-down views of APT reconstruction after anodic oxidation at 1.55 V for a–c) 60 s, d–f) 180 s, g–i) 300 s, showing the coverage of oxide (in blue) and hydroxy groups (in green) on the Ir (red) surface, and cross-sectional side views revealing the growth of oxide at j–n) 60 s, o–u) 180 s, and v–z) 300 s along the (002), (026), (024), (113), (115), (220), and (111) planes, respectively. The O iso-concentration surface (dark blue) in (b), (e) and (h) is 3.3 at. %, 67 at. %, 67 at. % respectively, indicating the location of the oxide clusters.

electrochemically oxidized tips in Figures 1 g and 3 b,e,h, respectively. All the Ir APT specimens in the present study were oriented along the [001] zone axis, revealing the (002), (113), (024), (113), and (115) poles. Sometimes the (220) and (111) poles are also observed (Figure 3 e) due to slight specimen displacement. The side view of the (002) plane, in Figure 1 g, exemplifies that all APT data were reconstructed to yield the interplanar spacing of Ir (002) planes (i.e., 0.19 nm). The reconstruction procedure was followed according to Ref. [23] and the reconstruction parameters for all APT data were detailed in Table S2. Additionally, the terrace edges can potentially function as active sites.[24] Thus, it is crucially important to distinguish the regions of terraces from the terrace edges. To resolve this information, we used a field ion microscopy image (FIM)[25] of Pt (Ir should yield similar patterns due to the similar atomic radius, crystal structure and atomic weight). Circular rings were drawn on the FIM image (Figure S4a) to delineate the terraces of high-indexed planes (blue for closed planes and green for open planes), while a yellow-shaded circular plate reveals the terrace edge of (002) planes. The atom maps (top-down view) in Figures 1 g and 3 b,e,h were overlayed with the ring pattern to discriminate between terraces and terrace edges of high-indexed and (002) planes, Figure S4b–e. Electrochemical oxide growth on the individual planes along the depth direction is shown in the side views in Figure 3 j–z (cropped from cross-sectional atom maps shown in Figure S5). All the side-view atom maps are selected within the circular rings identified in Figure S4c-e, which means that only the terraces were investigated in this study.

Different from the symmetric surface reconstructions occurring on APT tips during gas–solid reactions (at ≤ 573 K) reported in Refs [11e,13], the nucleation sites during electrochemical oxidation are highly selective. Asymmetric iridium oxides gradually grow between oxide nuclei, interconnecting

them, as seen from the top-down views (Figure 3 a,d,g). Specifically, after anodic polarization at 1.55 V for 60 s, we observed a higher coverage of oxides on the (024), (026), (113), and (115) planes, as indicated by O-rich regions which are highlighted by the O iso-concentration surfaces (blue) plotted in Figure 3 b. The oxide films on the (002), (026), (113), and (115) planes are comparably thin, limited to between two and six atomic layers (Figure 3 j,k,m,n), while a relatively thick oxide layer of ca. 6 nm grew along the (024) plane (Figure 3 l). To resolve hydroxy groups by APT in the electrochemically grown oxides, proton-free deuterated solvent (D_2O) and electrolyte ($DClO_4$) were used during the electrochemical treatments (step 4, Figure 1 e). This allows us to avoid the overlap with any residual hydrogen that may be present in the high vacuum chamber of the atom probe.[26] Figures 3 c and S5d–f show that the hydroxy groups formed during OER are distributed uniformly on the tip surface. It is noteworthy that the terrace edges, the region outside the circular rings in Figure S4c, are also covered by oxides. Investigating if OER first takes place on the step edge or the high-index plane requires a future correlative FIM/APT study. However, OER seems to occur dominantly on the terraces of the high-indexed planes (by comparing surface area of the oxidized regions on planes with those on terrace edges in Figure S4c).

As the anodic polarization time increases to 180 s, more surfaces become electrochemically oxidized and these oxides grow selectively on (026), (024), (220), and (111) planes and step edges of the (002) plane (see Figure 3 d,e). The oxide layer thickness on the (113), (115), (111), and (220) surfaces is only 2–3 nm, while it increases to 5–8 nm for the (002) and (024) surfaces (Figure 3 o–u). This is consistent with previous observations of Ir APT tips after very short thermal oxidation treatments, where the (024) and (002) planes were the first to be oxidized, while the (111) and (220) surfaces were oxidized

last.[22c] After 300 s of OER, the entire tip surface is oxidized, with most pronounced growth on the (026), (024), (113), and (115) planes (Figures 3 g–i and S5l–n). We observed that the oxide layer is more hydrated as more hydroxy groups are present at and near the surface (Figure 3i). Notably, the oxide layer on the (113) and (115) planes remains thin, i.e., 2–3 nm (Figure 3 y,z), while the oxide layer on the (024) and (026) planes grew 6–10 nm into the metallic bulk (Figure 3 w,x).

As shown in Figures 3 j–z, the thickness of the formed oxide strongly depends on the plane it grew on. Next, the evolution of the respective oxide compositions during the time of OER measurement was revealed by the one-dimensional composition profiles depicted in Figure 4 and Figure S6 (calculated along the white arrows in Figure S5d–n). At 60 s, the electrochemical oxide layers are so thin that the composition profiles (shown in Figures 4 a,b, S6a–c) reveal that the surface layers are mainly comprised of metallic Ir^0, which is in agreement with XPS data (Figure S3c). To analyze the oxide composition at 60 s, local mass spectra were obtained by placing analysis spheres (approx. 2 nm diameter) within the oxide films (see Figures S5d and S5f); these spectra show that the surface oxides on the (024) and (113) planes consist of sub-stoichiometric Ir−O species and hydroxy groups (Figure S7a,c). The IrO:OH ratio is close to 1:1, suggesting the formation of IrO−OH species which were also observed on the (026) and (115) planes, as detailed in Table 1. The coverage of IrO−OH, estimated by the ratio of IrO:Ir on the topmost atomic layer, and Gibbsian surface excess of O in the oxides formed on various planes are listed in Table S3. We can see that coverage of IrO−OH on the (024) plane was lower than that on the (113) plane, while the Gibbsian surface excess of oxygen in the oxide layer of (024) is slightly higher than (113). This is also confirmed by the presence of a large amount of atomic oxygen and Ir−O in the subsurface of the (024) plane shown in Figure S7b, indicating that the open plane enabled the penetration of electrolyte and electro-
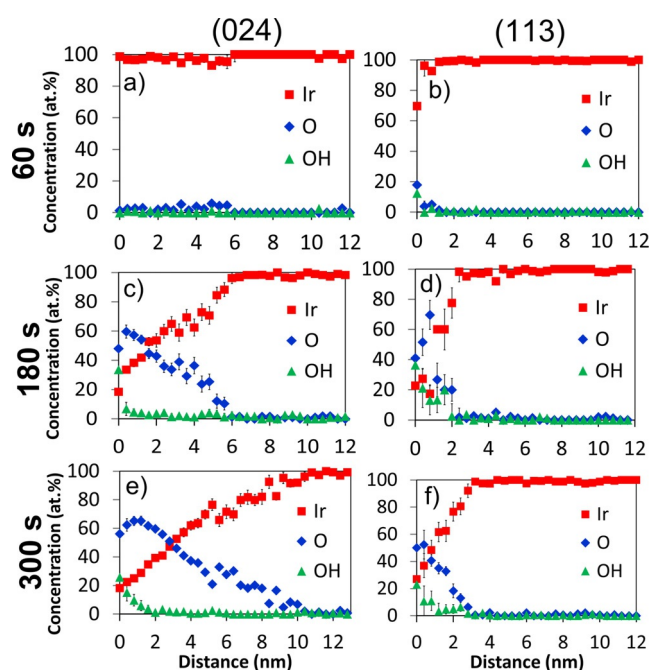
Figure 4. One-dimensional (1D) concentration profiles along the (024) and (113) planes in Figure 3 l,m,q,r,x,y (plotted along the white arrows marked in Figure S5d,f,g,i,n, respectively.) The error bars of the concentration are calculated from the square root of the total number of atoms of element *i* divided by the total number of all atoms.

chemical oxidation took place below the (024) plane (approx. 6 nm below the surface).

After anodic polarization for ≥180 s, the interface between the thick oxide layer, formed on the (002), (026), and (024) planes, and the metal substrate becomes rather diffuse, as compared to the thin oxide/metal interface across the more closed (113), (115), and (111) planes (Figure 4c–f, Figure S6d–k). Thus, we can categorize two different layers of oxides that grow on the open (026) and (024) planes: (i) the

Table 1: IrO:OH ratios in the thin surface oxide layer grown on the (002), (026), (024), (113), (115) planes after anodic oxidation at 1.55 V vs. RHE for 60 s, and an O:Ir ratio in the topmost 1–2 nm surface layer and subsurface of oxides formed on the (002), (026), (024), (113), (115), (220), (111) planes, and unoxidized or less oxidized regions after anodic oxidation at 1.55 V for 180 and 300 s derived from the 1D concentration profiles (Figure 4 and Figure S6) from the regions marked in Figure S5.

Conditions	(002)	(026)	(024)	(113)	(115)	(220)	(111)	Unoxidized or less oxidized region
60 s (IrO:OH ratio)	Adsorbed OH	1:1	1:1	1:1	1:1	–	–	Adsorbed OH
180 s Topmost 1–2 nm surface	2±0.3	2±0.1	2±0.2	1.9±0.2	2±0.1	2.2±0.2	2.1±0.2	Adsorbed OH
Subsurface (O:Ir ratio)	0.9±0.2	0.5±0.1	0.5±0.1	–	–	1.1±0.2	–	–
300 s Topmost 1–2 nm surface	1±0.1	2.8±0.2	2.9±0.2	2.3±0.2	2.2±0.2	–	–	1.1±0.1
Subsurface (O:Ir ratio)	–	0.5±0.1	1.1±0.2	–	–	–	–	–

topmost 2 nm (surface layer) and (ii) the subsurface layer. At 180 s, the O:Ir ratio (measured from the composition profiles in Figure 4c,d and Figure S6d–h and summarized in Table 1) is approximately 2:1 in the topmost 2 nm of the (002), (026), (024), and (220) planes, as well as within the thin surface oxide formed on the (113), (115), and (111) planes. This suggests that the composition of the top 2 nm of surface oxide on these planes is most likely IrO_2 combined with loosely bound hydroxy groups; this is further suggested by the local mass spectra given in Figure S7d,f.

As anodic polarization time increases to 300 s, the O:Ir ratio reaches 3 within the topmost 2 nm of the oxide layer on the (024) and (026) surfaces, and a ratio of 2–2.3 for the thin oxide layer that forms on the (113) and (115) planes (Figures 4e,f, S6i–k, as summarized in Table 1). $Ir^{+VI}O_3$ is possibly formed by Ir^{+IV} oxyhydroxide, as observed at 180 s. However, IrO_3 is short-lived and decomposes to oxygen and an Ir complex with a lower oxidation state.[17a,18a] Thus, the surface oxide is thought to contain $IrO_2 + O^•$, which is also in line with our XPS data that an increased amount of Ir^{+IV} was observed at 300 s (Figure S3d). In the subsurface region below the (112) plane, the amount of Ir–O species increases with OER measurement time (Figure S7e,h), resulting in the O:Ir ratio increasing to ca. 1:1 at 300 s (Table 1). It is noteworthy that, at both 60 and 180 s, the unoxidized surface is still covered by a thin layer of hydroxy groups (Figure S5f,i), and at 300 s, the less oxidized region consists of IrO–OH (Table 1, Figure S5l).

Our previous APT work[20] revealed that oxide nano-domains consisting of sub-stoichiometric Ir–O species along with hydroxy groups are first formed at the grain boundaries in polycrystalline iridium during OER. In the present study, we revealed that two distinct iridium oxides are formed on the open and closed planes of Ir tips. The temporal evolution of the Ir oxides on the open (e.g. (024)) and the closed (e.g. (113)) planes during OER is summarized in Figure 5. After 60 s of electrolysis at 1.55 V, the open and closed planes are both covered by 2–3 atomic layers of IrO–OH species (Figure 5a,b). This presence of such Ir^{III} species at the surface is also confirmed by XPS (Figure S3c). These Ir^{III}O–OH species can serve as OER precursors since the hydroxy groups can contribute to the oxygen evolution by combining with atoms from water via a peroxide mechanism.[27] Therefore, the short-time polarization "activates" the surfaces by forming Ir^{III}O–OH species; this is consistent with the previous observation that cycling the potential between 0.05 V and 1.6 V is the precondition for the formation of highly active, but also highly unstable, Ir^{+III} species.[6] As the OER proceeds, the topmost 1–2 nm active oxide layers on the open and closed planes evolve to less active IrO_2 (at 180 s, Figure 5c,d), $IrO_2 + O^•$ (at 300 s Figure 5e,f) along with hydroxy groups. The thickness of the oxide layer on the closed (113) plane remains at approximately 2 nm, while the oxide film grows continuously across the (024) planes to reach thicknesses of 8–10 nm. Importantly, we observed the sub-stoichiometric Ir–O in the (024) subsurface (Figures 3l and 5a) at the beginning of OER, and the amount of Ir–O species increases with OER measurement time (Figure 5c,e).

Open planes **Closed planes**

a) b) c) d) e) f)

Anodic oxidation time

Ir OH IrO IrO₂ IrO₃
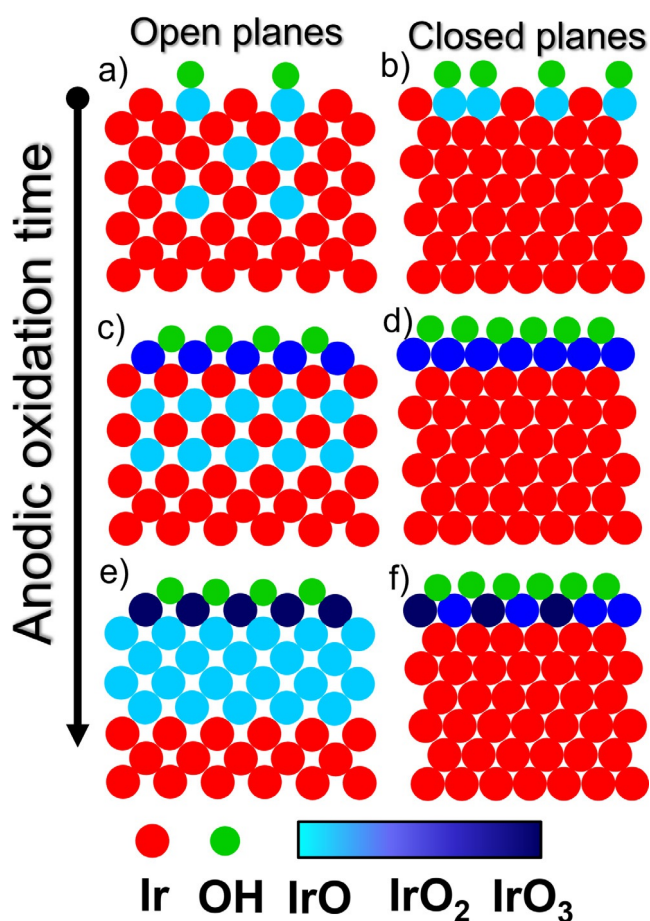
Figure 5. Schematic representation of the gradual changes observed during anodic polarization of (a, c, e) open planes, that is, (024) and (026), and (b, d, f) closed packed planes, that is, (113) and (115) Ir, under the OER conditions. After electrolysis for 60 s, IrO–OH species were formed on both open and closed planes. As the polarization proceeds, IrO_2 and $IrO_2 + O^•$ (denoted as IrO_3 in legend) denoted as along with loosely bound hydroxy groups grew on the topmost 1–2 nm surface layer of both open and closed planes. On the open planes, the subsurface gradually transformed into sub-stoichiometric Ir oxides.

The current literature has generally assumed that the double-layered oxide consists of a surface layer of porous hydrous oxide (IrO–OH) on top of a few monolayers of compact anhydrous IrO_2.[28] However, there is no direct experimental evidence to support the underlying mechanism by which this "sandwich structure" is formed. This is the result of severe experimental difficulties in detecting the chemistry of oxidized metal surfaces that exhibit surface and subsurface oxygen species embedded in metallic substrates. In this study, we use APT to reveal that a double-layered oxide structure is formed selectively on the open planes. Based on our results we propose the following formation mechanism for this double layer: electrolyte and molecular oxygen are thought to first diffuse underneath the (024) planes through place exchange, which initiates the gradual formation of metastable sub-stoichiometric IrO, instead of directly forming IrO_2.[28] The sub-stoichiometric IrO can enhance the electrocatalytic activity due to the adsorption of oxygen-containing radicals on sub-stoichiometric Ir–O being energetically favored.[29]

Thus, it is possible for the (024) plane to remain active as a consequence of the Ir−O species present in the subsurface, although the topmost surface is covered by IrO$_2$ (at 180 s and 300 s).[20] In contrast, no such subsurface oxide was observed below the closed planes, suggesting that the buried interface does not contribute to the surface reaction during OER. Thus, the oxide that grows on more closed packed planes is less active than oxide that grows on the open planes.

Previous work[5] confirms that the open (110) plane is more active compared to the closed (111) plane as Ir (110) shows a lower overpotential after the first scan of cyclic voltammetry, run between 1.2 V and 1.6 V vs. RHE at a scan rate of 5 mV s^{-1} (160 s per cycle). A recent study[6] reveals that the as-prepared Ir (210) yields a higher OER current density than that of Ir (111), and that high OER current density remains after 2 hours of chronoamperometry at 1.6 V. We believe that our study provides direct experimental evidence of surface/subsurface species that enhance the OER activity observed in the abovementioned studies.[5,6] Our results reveal that the topmost 1–2 nm surface layers of both open and closed planes consist of IrO$_2$ along with loosely bound hydroxy groups after 180 s, in line with their XPS data.[6] One can expect that a similar degree of oxidation would occur on both open and closed planes for longer durations of chronoamperometry. However, our results (Figures 3 v–z, 300 s of chronoamperometry) reveal continued oxidation on the (024) planes, while nearly no oxidation occurred on the closed planes (since the thickness of the oxide film is nearly unchanged). We speculate that the high-indexed open planes facilitate the incorporation of oxygen into the metal structure (Figure 3 l), which enables the formation of active Ir−O species at the diffuse oxide/metal interface. In comparison to closed packed planes, the relatively open (024) surface allows an easier penetration of electrolyte, enabling formation of substochiometric Ir−O species. Therefore, the open (024) surface has an extended structure whereby not only the surface, but also the subsurface volume is occupied by metastable Ir−O species, which potentially contributes continuously to the redox reactions during OER.[5,6,29] These nanosized features at specific locations are indiscernible by surface techniques like XPS since it provides the average electronic state of top few nm of a surface with limited lateral resolution. Furthermore, the previous study proposed that the initial surface planes might not be critical in determining their OER performance since individual Ir planes turn into similar inactive surface states after a long duration of chronoamperometry at a higher potential (1.7 V vs. RHE).[6] This would require a follow-up APT study to reveal the formation of surface species at similar conditions. The APT analysis of Ir tips after a longer duration (900 s) of chronoamperometry at 1.55 V was attempted. However, the Ir tips were covered by a thick layer of oxides and water molecules that caused abrupt fractures of specimens before bulk metallic Ir was revealed. Therefore, no correlation between surface species and nanofacets was obtained.

Conclusion

In summary, we studied the influence of different crystallographic planes on the formation of oxide species during OER conditions utilizing the highly catalytically active Ir system. We reveal the presence of metastable substoichiometric Ir−O species in the subsurface of high-indexed open planes, such as the (024) plane. The presence of these species is thought to provide an enhanced OER activity. In contrast, the topmost layer of closed planes (e.g., (113)) evolves into stable oxide species, like IrO$_2$, potentially resulting in a lower catalytic activity. Overall, our new observations shed light on the interplay between morphology and activity of Ir during OER electrocatalysis. We propose that tetrahexahedron-shaped Ir nanoparticles that are enclosed by open planes can yield a potentially optimal activity. Importantly, we present a novel methodology for directly interrogating the surface electronic state and composition of different oxides that are present on the same electrode. The benefit of our approach is that a single APT tip offers multiple crystallographic planes for 3D characterization of elemental distribution and compositions in the surface and near-surface regions, at the atomic scale. Our innovative approach, here exemplified by investigating Ir, will be extended in future work to investigate other metal/alloy, oxide, or complex layered structures for OER and other important reactions.

Conflict of Interest

The authors declare no conflict of interest.

[1] M. Carmo, D. L. Fritz, J. Mergel, D. Stolten, *Int. J. Hydrogen Energy* **2013**, *38*, 4901 – 4934.

[2] N.-T. Suen, S.-F. Hung, Q. Quan, N. Zhang, Y.-J. Xu, H. M. Chen, *Chem. Soc. Rev.* **2017**, *46*, 337 – 365.

[3] a) G. Beni, L. Schiavone, J. Shay, W. Dautremont-Smith, B. Schneider, *Nature* **1979**, *282*, 281; b) T. Reier, M. Oezaslan, P. Strasser, *ACS Catal.* **2012**, *2*, 1765 – 1772; c) S. Cherevko, S. Geiger, O. Kasian, N. Kulyk, J.-P. Grote, A. Savan, B. R. Shrestha, S. Merzlikin, B. Breitbach, A. Ludwig, *Catal. Today* **2016**, *262*, 170 – 180.

[4] K. A. Stoerzinger, L. Qiao, M. D. Biegalski, Y. Shao-Horn, *J. Phys. Chem. Lett.* **2014**, *5*, 1636 – 1641.

[5] E. Özer, C. Spöri, T. Reier, P. Strasser, *ChemCatChem* **2017**, *9*, 597 – 603.

[6] M. Scohy, S. Abbou, V. Martin, B. Gilles, E. Sibert, L. Dubau, F. Maillard, *ACS Catal.* **2019**, *9*, 9859 – 9869.

[7] R. Narayanan, M. A. El-Sayed, *Nano Lett.* **2004**, *4*, 1343 – 1348.

[8] V. Pfeifer, T. E. Jones, J. J. Velasco Vélez, C. Massué, R. Arrigo, D. Teschner, F. Girgsdies, M. Scherzer, M. T. Greiner, J. Allan, M. Hashagen, G. Weinberg, S. Piccinin, M. Hävecker, A. Knop-Gericke, R. Schlögl, *Surf. Interface Anal.* **2016**, *48*, 261 – 273.

[9] A. Minguzzi, O. Lugaresi, E. Achilli, C. Locatelli, A. Vertova, P. Ghigna, S. Rondinini, *Chem. Sci.* **2014**, *5*, 3591 – 3597.

[10] a) C. Eley, T. Li, F. Liao, S. M. Fairclough, J. M. Smith, G. Smith, S. C. E. Tsang, *Angew. Chem. Int. Ed.* **2014**, *53*, 7838 – 7842; *Angew. Chem.* **2014**, *126*, 7972 – 7976; b) T. Li, P. A. Bagot, E. Christian, B. R. Theobald, J. D. Sharman, D. Ozkaya, M. P. Moody, S. E. Tsang, G. D. Smith, *ACS Catal.* **2014**, *4*, 695 – 702; c) P. Felfer, P. Benndorf, A. Masters, T. Maschmeyer, J. M. Cairney, *Angew. Chem. Int. Ed.* **2014**, *53*, 11190 – 11193; *Angew. Chem.* **2014**, *126*, 11372 – 11375; d) S.-H. Kim, P. W. Kang, O. O. Park, J.-B. Seol, J.-P. Ahn, J. Y. Lee, P.-P. Choi, *Ultramicroscopy* **2018**, *190*, 30 – 38; e) Z. Ji, T. Li, O. M. Yaghi, *Science* **2020**, *369*, 674 – 680; f) A. Devaraj, M. Gu, R. Colby, P. Yan, C. M. Wang, J. Zheng, J. Xiao, A. Genc, J. Zhang, I. Belharouak, *Nat. Commun.* **2015**, *6*, 8014.

[11] a) C. Voss, N. Kruse, *Appl. Surf. Sci.* **1995**, *87*, 127 – 133; b) C. Voss, N. Kruse, *Appl. Surf. Sci.* **1996**, *94*, 186 – 193; c) T. Visart de Bocarmé, N. Kruse, *Chaos* **2002**, *12*, 118 – 130; d) C. Barroo, Y. De Decker, T. Visart de Bocarmé, N. Kruse, *J. Phys. Chem. C* **2014**, *118*, 6839 – 6846; e) P. Bagot, A. Cerezo, G. Smith, *Surf. Sci.* **2007**, *601*, 2245 – 2255.

[12] A. Moore, *J. Phys. Chem. Solids* **1962**, *23*, 907 – 912.

[13] P. A. Bagot, T. Visart de Bocarmé, A. Cerezo, G. D. Smith, *Surf. Sci.* **2006**, *600*, 3028 – 3035.

[14] a) T. Li, P. A. Bagot, E. A. Marquis, S. E. Tsang, G. D. Smith, *J. Phys. Chem. C* **2012**, *116*, 4760 – 4766; b) T. Li, E. Marquis, P. Bagot, S. Tsang, G. Smith, *Catal. Today* **2011**, *175*, 552 – 557.

[15] a) R. Kötz, H. Neff, S. Stucki, *J. Electrochem. Soc.* **1984**, *131*, 72 – 77; b) J. Augustynski, M. Koudelka, J. Sanchez, B. Conway, *J. Electroanal. Chem. Interfacial Electrochem.* **1984**, *160*, 233 – 248.

[16] K. Schweinar, R. L. Nicholls, C. R. Rajamathi, P. Zeller, M. Amati, L. Gregoratti, D. Raabe, B. Greiner, B. Gault, O. Kasian, *J. Mater. Chem. A* **2020**, *8*, 388 – 400.

[17] a) R. Kötz, H. Lewerenz, P. Brüesch, S. Stucki, *J. Electroanal. Chem. Interfacial Electrochem.* **1983**, *150*, 209 – 216; b) V. Pfeifer, T. Jones, J. V. Vélez, C. Massué, M. Greiner, R. Arrigo, D. Teschner, F. Girgsdies, M. Scherzer, J. Allan, *Phys. Chem. Chem. Phys.* **2016**, *18*, 2292 – 2296.

[18] a) S. Cherevko, S. Geiger, O. Kasian, A. Mingers, K. J. Mayrhofer, *J. Electroanal. Chem.* **2016**, *773*, 69 – 78; b) S. Geiger, O. Kasian, B. R. Shrestha, A. M. Mingers, K. J. Mayrhofer, S. Cherevko, *J. Electrochem. Soc.* **2016**, *163*, F3132 – F3138.

[19] D. F. Abbott, D. Lebedev, K. Waltar, M. Povia, M. Nachtegaal, E. Fabbri, C. Copéret, T. J. Schmidt, *Chem. Mater.* **2016**, *28*, 6591 – 6604.

[20] T. Li, O. Kasian, S. Cherevko, S. Zhang, S. Geiger, C. Scheu, P. Felfer, D. Raabe, B. Gault, K. J. J. Mayrhofer, *Nat. Catal.* **2018**, *1*, 300.

[21] D. J. Larson, T. J. Prosa, R. M. Ulfig, B. P. Geiser, T. F. Kelly, *Local Electrode Atom Probe Tomography: A User's Guide*, Springer, New York, **2013**.

[22] a) Y. Chen, D. Seidman, *Surf. Sci.* **1971**, *27*, 231 – 255; b) F. Vurpillot, A. Bostel, D. Blavette, *J. Microsc.* **1999**, *196*, 332 – 336; c) M. Fortes, B. Ralph, *Proc. R. Soc. London Ser. A* **1968**, *307*, 431 – 448.

[23] a) B. Gault, D. Haley, F. de Geuser, M. P. Moody, E. A. Marquis, D. J. Larson, B. P. Geiser, *Ultramicroscopy* **2011**, *111*, 448 – 457; b) B. Gault, F. De Geuser, L. T. Stephenson, M. P. Moody, B. C. Muddle, S. P. Ringer, *Microsc. Microanal.* **2008**, *14*, 296 – 305.

[24] J. H. Pfisterer, Y. Liang, O. Schneider, A. S. Bandarenka, *Nature* **2017**, *549*, 74 – 77.

[25] https://en.wikipedia.org/wiki/Field_ion_microscope.

[26] Y.-S. Chen, D. Haley, S. S. Gerstl, A. J. London, F. Sweeney, R. A. Wepf, W. M. Rainforth, P. A. Bagot, M. P. Moody, *Science* **2017**, *355*, 1196 – 1199.

[27] O. Kasian, S. Geiger, T. Li, J.-P. Grote, K. Schweinar, S. Zhang, C. Scheu, D. Raabe, S. Cherevko, B. Gault, *Energy Environ. Sci.* **2019**, *12*, 3548 – 3555.

[28] a) S. Cherevko, S. Geiger, O. Kasian, A. Mingers, K. J. Mayrhofer, *J. Electroanal. Chem.* **2016**, *774*, 102 – 110; b) P. G. Pickup, V. Birss, *J. Electroanal. Chem. Interfacial Electrochem.* **1987**, *220*, 83 – 100.

[29] T. Binninger, R. Mohamed, K. Waltar, E. Fabbri, P. Levecque, R. Kötz, T. J. Schmidt, *Sci. Rep.* **2015**, *5*, 12167.